Journal of Materials Chemistry A

ROYAL SOCIETY OF CHEMISTRY

PAPER

Published on 06 October 2026
Licensed under CC-BY 4.0

Check for updates

Cite this: *J. Mater. Chem. A*, 2026, **14**, 44625

Role of structural disorder and aggregation in shaping the redox and optical properties of the small molecular acceptor Y6 in the bulk phase

Mateus Bergami, [a] Leandro R. Franco[b] and C. Moyses Araujo*[ac]

Received 2nd August 2026
Accepted 21st September 2026

DOI: 10.1039/d6ta06533c

rsc.li/materials-a

Non-fullerene acceptors such as Y6 have enabled remarkable advances in organic photovoltaics, yet a quantitative understanding of their electronic properties in the bulk phase remains challenging due to the combined effects of structural disorder and molecular packing. Here, a comprehensive multiscale investigation of Y6 films by integrating molecular dynamics simulations, sequential QM/MM calculations, and optimally tuned range-separated hybrid density functional theory is presented. Structural disorder is shown to play a dominant role in shaping the electronic landscape, leading to broad distributions of excitation energies and significantly improved agreement with experimental redox potentials and the optical spectrum. Furthermore, explicit inclusion of molecular packing refines these properties by promoting intermolecular polarization and electronic delocalization, which are essential for accurately describing exciton binding energies. Notably, good agreement with experimental exciton binding energies is achieved with a quantum region comprising fewer molecules than previously suggested, arising from the complementary effects of explicit intermolecular interactions and structural disorder. Analysis of excited states reveals the emergence of intermolecular charge-transfer character driven by specific donor–acceptor stacking motifs, providing a molecular-level understanding of charge separation in Y6 films. These results provide a predictive multiscale framework for understanding and engineering excitonic processes in non-fullerene acceptor materials.

1 Introduction

Non-fullerene acceptors (NFAs) have fundamentally reshaped the landscape of organic solar cells, enabling single-junction power conversion efficiencies exceeding 20% across diverse active-layer designs, including all-polymer blends and multi-component ternary and quaternary systems, through molecular and morphological strategies that combine strong and tunable optical absorption, finely tuned frontier energy levels, and favorable solid-state organization.[1–7] Among the wide range of NFAs developed to date, Y6 has emerged as a prototypical benchmark system, whose outstanding photovoltaic performance underscores both the promise and the complexity of modern organic semiconductors.[8–10] Its extended fused-ring backbone, pronounced molecular planarity, and fluorinated end groups promote broad near-infrared absorption, efficient electron transport when blended with donor polymers, and dense solid-state packing motifs, such as face-on orientations and pronounced π–π stacking.[11,12] These structural features are widely associated with enhanced exciton diffusion and efficient charge separation in the solid state.[13–16]

Despite its success, Y6 also exemplifies a central theoretical challenge in organic semiconductor research. Its electronic properties are governed not exclusively by isolated molecules but by collective electronic responses arising from a dense, intrinsically disordered film environment. Thin films of Y6 exhibit substantial structural heterogeneity, characterized by broad distributions of intermolecular distances, relative orientations, and local packing motifs that fluctuate dynamically over multiple length scales.[17,18] These features critically modulate polarization screening, intermolecular charge transfer interactions, and exciton delocalization, yet they are difficult to capture within conventional theoretical approaches. As a result, calculations based on optimized single-molecule geometries often fail to reproduce experimental redox potentials, optical gaps, and exciton binding energies, thereby limiting their predictive power for device-relevant properties.[19–21]

Recent theoretical and computational studies have increasingly converged on the conclusion that explicit inclusion of structural disorder and environmental effects is essential for a realistic description of NFA films. Kupgan *et al.* demonstrated that Y6 exhibits distinctive local packing motifs compared to earlier ITIC derivatives, with pronounced short-range order that

[a]*Department of Engineering and Physics, Karlstad University, SE-65188 Karlstad, Sweden*

[b]*Laboratory for Chemistry of Novel Materials, University of Mons, Place du Parc, 20, 7000 Mons, Belgium*

[c]*Materials Theory Division, Department of Physics and Astronomy, Uppsala University, Sweden. E-mail: moyses.araujo@kau.se*

directly impacts its electronic couplings and energetic landscape.[17] More recently, Franco *et al.* showed, through a multiscale investigation of a conjugated donor–acceptor polymer in the bulk phase, that disorder and environmental anisotropy shape both ground- and excited-state properties, and that neglecting these effects leads to systematic deviations from experimental observables.[21] Complementarily, Tamura employed a quantum mechanics/molecular mechanics (QM/MM) framework to study PM6–Y6 blends, revealing that disorder-induced energetic landscapes and quadrupole-driven electrostatic effects give rise to spontaneous potential cascades that facilitate charge separation, while also highlighting marked differences relative to PM6–ITIC systems.[22] Together, these studies establish that disorder and environment are non-negligible elements of the electronic structure of NFA-based materials, rather than secondary perturbations.

Building on this emerging consensus, multiscale modeling approaches that integrate molecular dynamics (MD) simulations, QM/MM methodologies, and excited state electronic structure calculations have become indispensable tools for addressing the complexity of organic semiconductor films. In particular, the recent multiscale framework applied to PF5–Y5 polymeric films by Franco *et al.* achieved quantitative agreement with experimental redox potentials and optical properties by explicitly accounting for structural disorder and environmental screening in the bulk phase.[21] However, a systematic assessment of how disorder, molecular packing structure, and the QM region size jointly control the electronic structure of small-molecule NFAs remains largely unexplored. Akram *et al.* suggested that relatively large molecular clusters (on the order of six to seven molecules) are required to accurately describe key quantities such as exciton binding energies of Y6 films.[23] In contrast, we demonstrate that a quantitatively consistent description can already be achieved with smaller clusters when structural disorder is explicitly included. This indicates that the apparent requirement for large QM regions may, in part, reflect the absence of explicit disorder sampling, and highlights that disorder effects can play a role comparable to, or even more significant than, QM region size in determining electronic properties. In the present work, we apply the protocol proposed by Franco *et al.*[21] to Y6 bulk, a substantially more aggregation-prone and electronically delocalized environment, and explicitly probe the impact of its central methodological elements, namely disorder sampling, QM region expansion, and dielectric screening, on the electronic properties of the bulk phase. It should be emphasized that the present simulations do not include explicit substrate, electrode, air interfaces and therefore represent the bulk condensed phase rather than the complete morphology of an experimental thin film. Such interfaces may influence local molecular orientation, packing, and dielectric screening. Consequently, comparison with thin-film measurements should primarily be interpreted as an assessment of the extent to which bulk-like structural and dielectric effects account for the experimentally observed electronic properties.

Employing this multiscale strategy to Y6 bulk enables us to address several critical aspects that have not been explored in previous theoretical studies of NFAs. First, we explicitly incorporate large QM regions comprising up to four Y6 molecules, enabling a direct and systematic description of intermolecular polarization, electronic delocalization, and packing-induced effects on both ground- and excited-state properties. In combination with explicit disorder sampling, this allows us to disentangle the respective roles of QM region size and structural heterogeneity in determining electronic properties. Second, these large QM regions are embedded within a polarizable continuum model (PCM) parameterized using experimentally determined static and dynamic dielectric constants of Y6 films, providing a physically consistent representation of long-range dielectric screening. This combined treatment enables a systematic separation of local aggregation effects from collective environmental polarization, thereby clarifying their respective roles in governing the electronic structure of the bulk phase.

By analyzing statistically representative MD snapshots, we demonstrate that the simultaneous inclusion of structural disorder and molecular packing systematically and significantly improves calculated redox potentials, fundamental gap, optical gap, UV-Vis spectrum and exciton binding energies, bringing theoretical predictions into close quantitative agreement with experimental measurements. Notably, accurate exciton binding energies are recovered without requiring the very large molecular clusters previously suggested, demonstrating that structural disorder strongly affects the resulting exciton binding energies in the bulk phase. Beyond average energetic trends, the use of large QM regions provides direct access to the nature of excited states under realistic aggregation conditions. We show that local packing motifs and relative molecular orientations have an impact on the character of the lowest singlet excited state (S_1). While ground state energetics and the optical gap display only limited sensitivity to these motifs, the S_1 exhibits a markedly enhanced intermolecular charge-transfer character in strongly coupled configurations, revealing how the bulk structure selectively governs the excited state electronic structure and charge separation pathways.

In combination, our results provide a quantitative understanding of how disorder, molecular packing structure, and dielectric environment collectively shape the electronic landscape of Y6 bulk. More broadly, this work demonstrates that the interplay between structural disorder and finite-size QM descriptions must be properly accounted for to capture the physics of non-fullerene acceptors. By explicitly bridging molecular packing, molecular structure, and excited state character, our study reinforces the central role of multiscale modeling in advancing the theory of organic photovoltaic materials.

2 Computational methodology

The multiscale approach adopted in this work follows the protocol recently proposed by Franco *et al.* for simulating solution-processed organic semiconductor films *via* solvent evaporation, which provides a physically realistic description of bulk structure and electronic properties.[21] In the present study, this methodology is applied to the small-molecule non-fullerene acceptor Y6.

 This journal is © The Royal Society of Chemistry 2026

2.1 Molecular dynamics simulations

Classical molecular dynamics simulations were employed to model the formation of Y6 bulk from solution. The ground-state geometry of an isolated Y6 molecule was optimized in the gas phase using density functional theory (DFT) with the B3LYP exchange–correlation functional and the 6-311G(d,p) basis set employing Gaussian 16 software.[24] Atomic partial charges were derived at the same level of theory using the CHELPG scheme.[25] Bonded and non-bonded interactions were described using the OPLS-AA force field, with parameters generated using LigParGen.[26,27] In addition, specific dihedral terms were introduced to improve the force field and at the same time preserve the planarity of the conjugated core, as detailed in the SI.

The initial solution-phase configuration was constructed by randomly placing 150 Y6 molecules, in their optimized geometries, within a cubic simulation box using the Packmol software, enforcing a minimum atomic distance of 5 Å.[28] This molecular assembly was subsequently merged with an equilibrated chloroform solvent box, corresponding to the solvent employed in the experimental processing of Y6 films.[9,29,30] Overlapping solute–solvent molecules were removed using a van der Waals scaling procedure, and the resulting Y6-chloroform solution, composed of 150 Y6 molecules and 20 992 solvent molecules, was equilibrated for 10 ns under isothermal–isobaric (NPT) conditions at room temperature ($T =$ 298.15 K) and pressure ($p = 1$ atm), using a chloroform isothermal compressibility of 9.9×10^{-5} bar^{-1}. All MD simulations were performed using the GROMACS 2023.4 software package.[31] Temperature was controlled using the V-rescale thermostat with a coupling constant of 0.1 ps, while pressure was regulated using the C-rescale barostat with a coupling constant of 2 ps.[32,33] Non-bonded interactions were evaluated within a cutoff radius of 1.4 nm, and long-range electrostatic interactions were treated using the smooth particle-mesh Ewald (PME) method with cubic interpolation and a Fourier spacing of 0.14 nm.[34] The equations of motion were integrated using the leapfrog algorithm with a time step of 2 fs, and all bonds involving hydrogen atoms were constrained using the LINCS algorithm.[35] In addition, the center of mass translational motion was removed every 100 simulation steps.

The equilibrated solution served as the starting point for the solvent evaporation simulations. Solvent removal was carried out using the iterative evaporation protocol proposed by Franco *et al.*,[21] in which a fixed fraction of randomly selected chloroform molecules was removed at each evaporation cycle. In the present work, the evaporation rate was set to 0.5% of the total number of solvent molecules present at the beginning of the evaporation procedure, corresponding to a slow solvent-removal regime designed to enhance solute–solvent equilibration and minimize artificial structural fluctuations during the evaporation. After each solvent-removal step, the system was subjected to a simulated annealing stage under canonical ensemble (NVT) conditions for 1 ns, followed by a 1 ns structural relaxation under NPT conditions at 298.15 K and 1 atm. During the NVT simulated annealing stage, the temperature was gradually increased from 298.15 K to 373.15 K over the first 0.1 ns, maintained at 373.15 K for 0.8 ns, and subsequently reduced back to 298.15 K during the final 0.1 ns. The use of simulated annealing under NVT conditions prevents artificial density reduction during solvent removal and promotes efficient structural reorganization during bulk formation. This heating–cooling procedure was designed to mimic the gradual solvent evaporation and molecular rearrangement occurring during experimental processing conditions. The evaporation cycles were repeated until complete solvent removal was achieved. Six independent evaporation simulations were performed using different initial velocity distributions in order to generate statistically independent Y6 bulk trajectories and improve configurational sampling of the disordered condensed phase. The technical details of the QM/MM protocol, including snapshot selection, definition of the QM region, and treatment of environmental screening effects, are described in the following section. A schematic overview of the evaporation protocol and the sequential QM/MM workflow adopted in this work is presented in Fig. 1.

2.2 Sequential QM/MM procedure

The electronic properties of Y6 bulk were investigated using a sequential QM/MM (s-QM/MM) methodology, in which statistically representative configurations are first generated through classical MD simulations and subsequently subjected to quantum-mechanical calculations. In the present approach, the MM environment is not retained as explicit point charges during the QM calculations employing the electrostatic embedding. Instead, structural effects of the environment are inherited from the MD sampling, while the average dielectric response of the Y6 bulk is described through PCM. For the larger QM regions, the explicit inclusion of neighboring Y6 molecules additionally captures part of the local anisotropy associated with their molecular arrangements and intermolecular interactions.[36–38]

To ensure robust statistical sampling of the disordered Y6 bulk, configurations were extracted from the six independent MD trajectories obtained after solvent evaporation and equilibration. The convergence and reproducibility of the resulting bulk structures were further assessed from the density evolution during solvent evaporation and from center-of-mass radial distribution functions and coordination-number profiles for the six independent trajectories as presented in the SI. These analyses show highly consistent density and intermolecular structural characteristics across the independently generated systems. Moreover, the resulting average bulk density of 1.15 g cm^{-3} lies within the range reported for experimentally determined Y6 single-crystal structures (approximately 1.10–1.32 g cm^{-3}), further supporting the physical consistency of the simulated condensed phase.[39,40]

From each trajectory, 50 configurations were selected at 1 ns intervals, yielding a total ensemble of 300 snapshots representative of the bulk structural heterogeneity. The combination of multiple independent simulations and time-separated sampling minimizes correlations between configurations and provides extensive coverage of configurational space. This

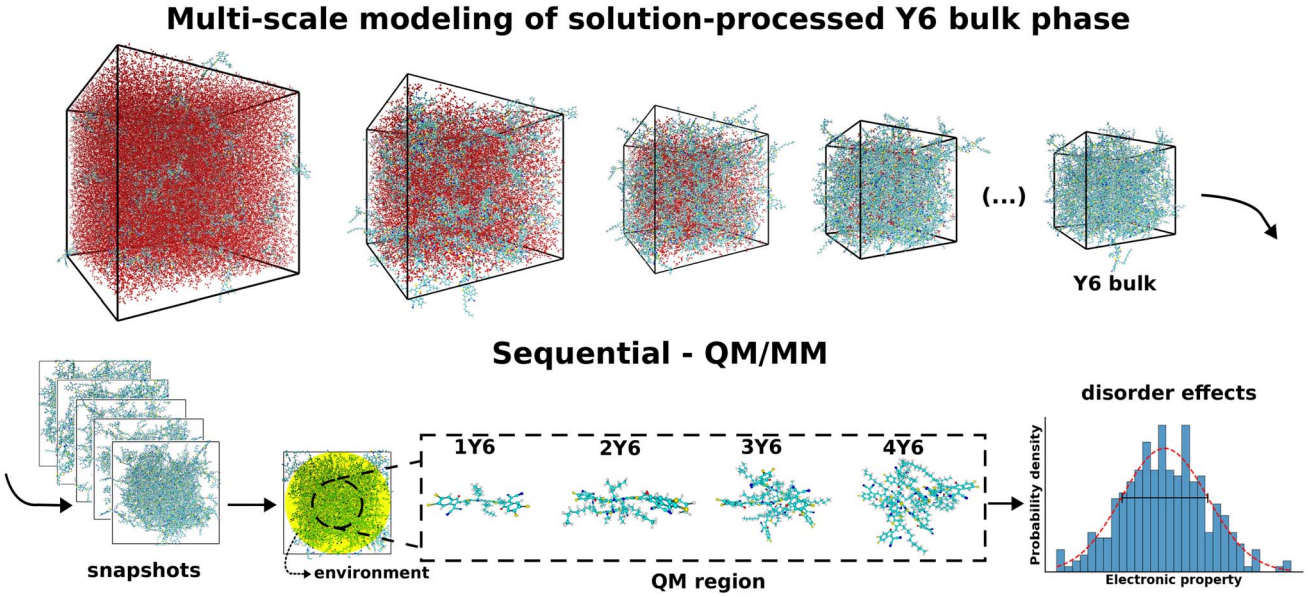

Fig. 1 Schematic illustration of the multiscale modeling protocol adopted in this work. The top panel depicts the solvent evaporation process, highlighting the gradual reduction of the simulation box until a solvent-free Y6 bulk is obtained. The bottom panel illustrates the sequential QM/MM procedure, including the selection of QM regions using the center-of-mass criteria from MD snapshots, and the resulting distribution of electronic properties arising from structural disorder in the Y6 bulk.

sampling strategy is essential for capturing disorder-induced variations in electronic properties, which play a central role in the present work. For each trajectory, the 50 extracted configurations were associated with different Y6 molecules selected from the 150 molecules present in the simulation box, which were used as a reference molecule for the construction of the QM region. This procedure ensures that the QM calculations probe distinct spatial regions of the bulk and are not biased toward a specific local environment. As a result, the final ensemble captures both temporal and spatial disorder inherent to the Y6 bulk structure.

The QM region was then defined for each selected configuration. In the smallest QM region, the reference Y6 molecule was treated at the quantum-mechanical level, while the average dielectric response of the surrounding bulk environment was represented using PCM parameterized with the experimental static ($\varepsilon_s = 3.3$) and dynamic ($\varepsilon_d = 5.3$) dielectric constants of the Y6 film.[41] To explicitly investigate the role of aggregation and intermolecular interactions, larger QM regions were also constructed by including two, three, and four Y6 molecules in the QM subsystem. In these cases, additional Y6 molecules were selected based on their center-of-mass distance from the reference molecule, ensuring inclusion of nearest-neighbor molecules representative of realistic packing motifs and intermolecular coupling environments. For each snapshot and QM-region size, the PCM cavity was independently constructed from all atoms explicitly included in the corresponding QM region, following the same cavity-definition criteria. Accordingly, the average cavity volumes increase from (1942.3 ± 8.3) Å^3 for QM(1Y6) to (3844.7 ± 20.4), (5745.8 ± 29.8), and (7643.3 ± 35.1) Å^3 for QM(2Y6), QM(3Y6), and QM(4Y6), respectively. The dielectric parameters were kept unchanged because the continuum surrounding each explicit QM region represents the same bulk Y6 dielectric environment. This distance-based criterion provides an unbiased and general approach to sampling Y6 bulk configurations, yielding an ensemble of QM regions spanning a wide range of relative orientations, contact patterns, and intermolecular coupling strengths, as illustrated in Fig. 1. These configurations form the basis for the quantum-mechanical calculations discussed in the following section.

2.3 Electronic structure of ground and excited states

Electronic-structure calculations were performed within the framework of DFT using a screened range-separated hybrid (SRSH) approach based on the long-range corrected LC-ωHPBE functional.[42–46] This class of functionals is particularly well suited for describing frontier energy levels and charge-transfer states in organic semiconductors, as it enables a physically motivated treatment of exchange interactions and dielectric screening.[47] In this work, an optimal tuning strategy that explicitly accounts for the dielectric environment of the Y6 film was employed using the PCM model, referred to as the OT-SRSH-PCM approach.

The optimal tuning procedure was carried out in two stages. First, the range-separation parameter ω was optimized for an isolated Y6 molecule in the gas phase by minimizing deviations from Koopmans' theorem, ensuring a consistent description of ionization potentials and electron affinities. Subsequently, ω was kept fixed, and the short- and long-range Hartree–Fock exchange fractions (α and β) were optimized in the presence of the PCM, subject to the constraint $\alpha + \beta = 1/\varepsilon$, where ε is the experimental static dielectric constant of the Y6 film. This condition ensures that the functional incorporates the

 This journal is © The Royal Society of Chemistry 2026

appropriate level of dielectric screening characteristic of the bulk environment. The results of the optimal tuning procedure are presented in the SI.

Vertical oxidation and reduction energies were computed using a ΔSCF approach based on ground-state total energy differences. For each configuration and QM region, single-point DFT calculations were performed for the neutral, cationic, and anionic charge states at the same nuclear geometry and structural relaxation of the charged states was not included. The oxidation potential was obtained from the total energy difference between the cationic and neutral states, while the reduction potential was obtained from the difference between the neutral and anionic states. The fundamental gap was then defined as the difference between the oxidation and reduction potentials. For the optimized geometry, these quantities correspond to single values obtained from one configuration. In contrast, for the bulk snapshot calculations based on the s-QM/MM protocol, oxidation and reduction potentials were evaluated for all 300 configurations in the ensemble and subsequently averaged to obtain statistically meaningful bulk values.

Excited-state properties were computed using time-dependent DFT (TD-DFT) within the same OT-SRSH-PCM framework. Vertical excitation energies were evaluated for each snapshot at the neutral ground-state geometry, consistent with optical absorption processes. For all QM regions, the vertical excitation energy of the S_1 was computed and used to define the optical gap for each configuration. In addition, for the simplest QM region containing a single Y6 molecule, the lowest 50 singlet excited states were calculated in order to construct the ensemble-averaged UV-Vis absorption spectrum. The ensemble-averaged UV-Vis spectrum was obtained by convoluting the vertical excitation energies and oscillator strengths over all sampled configurations, thereby explicitly accounting for disorder-induced broadening and variability in the optical response of the Y6 film. Exciton binding energies were subsequently obtained as the difference between the fundamental and optical gaps. This definition, combined with explicit disorder sampling, enables a direct assessment of how excitonic properties converge with respect to QM region size. For all electronic properties computed from the ensemble of disordered configurations, including oxidation and reduction potentials, fundamental gap, optical gap, excitation energies, and exciton binding energy, energetic disorder was quantified following the statistical procedure reported by Kupgan *et al.*[48] Probability density distributions were constructed from the set of values obtained across the ensemble of configurations and subsequently fitted to Gaussian functions. The mean values extracted from these fits correspond to ensemble-averaged electronic properties of the Y6 bulk, while the associated standard deviations provide a quantitative measure of energetic disorder arising from structural heterogeneity.

The OT-SRSH-PCM functional was applied consistently to all QM regions defined within the s-QM/MM framework, including single-molecule and aggregated (two-, three-, and four-molecule) QM regions. Ground-state and excited-state properties were thus treated at the same level of theory, enabling a coherent and internally consistent assessment of the combined effects of structural disorder, molecular packing, and dielectric screening on the electronic properties of Y6 bulk. While optimal tuning of range-separated hybrid functionals is known to yield highly accurate electronic properties, repeated tuning for systems of increasing size can introduce systematic errors, as the resulting functional tends to become increasingly semi-local.[49–52] In the present work, this limitation is mitigated because all aggregated QM regions are constructed from the same molecular building block, Y6. Consequently, tuning the range-separation parameter once for the isolated Y6 molecule establishes the appropriate physical length scale for long-range exchange, which can then be consistently applied to larger QM regions without further re-optimization. The validity of this approximation was further assessed by comparing the ensemble-averaged HOMO and LUMO energies with the corresponding vertical oxidation and reduction energies for each QM-region size in the SI. Deviations remain below 0.1 eV from QM(1Y6) to QM(4Y6), supporting the use of the same optimally tuned parameters as a good approximation for the larger QM regions. This strategy has been successfully employed in previous studies of complex light-harvesting systems, including investigations of primary charge separation in biological reaction centers, and has recently been demonstrated to be reliable for Y6 bulk, where the same approach was used to analyze electronic excitations and exciton binding energies for Y6 aggregates.[23,53] All electronic-structure calculations were performed using the Gaussian 16 software package.[24] Additional computational details and results of the optimal tuning procedure are provided in the SI. This framework enables a systematic evaluation of the interplay between structural disorder, molecular packing structure, and QM region size, which is a central focus of the present study.

3 Results and discussion

In this section, we present and discuss the results obtained from the multiscale modeling of Y6 bulk, following the workflow presented in the Computational methodology section. We first analyze the structural features emerging from the solvent-processed bulk, with particular emphasis on intermolecular packing and disorder. These structural insights provide the foundation for understanding the electronic properties discussed in the subsequent subsections, including redox energetics, frontier orbitals distribution, UV-Vis spectrum, excited-state characteristics, and exciton binding energies.

3.1 Molecular-level structural analysis

We begin by analyzing the intermolecular packing motifs present in the Y6 bulk, focusing on dimer configurations extracted from the s-QM/MM sampling. Particular attention is given to the occurrence of close intermolecular contacts and their relationship to face-on molecular orientations, which have been identified as a defining structural feature of Y6-based films and are closely linked to efficient electronic coupling and charge transport.[9,30]

To characterize intermolecular interactions, we adopt the criterion whereby a close contact is defined as any interatomic distance between atoms belonging to two different Y6 molecules that is equal to or smaller than 4.0 Å. The analysis is restricted to backbone atoms of both molecules in the dimer. Configurations exhibiting 25 or more close contacts are classified as face-on relative orientation, consistent with previous studies.[17] This definition provides a robust and physically meaningful descriptor of intermolecular proximity and packing structure.

Applying this analysis to the ensemble of 300 Y6 dimer configurations considered in the QM calculations reveals a strong tendency toward intermolecular association in the bulk film. Specifically, 254 configurations (approximately 85% of the ensemble) exhibit at least one close contact between atoms belonging to the backbone of different molecules, indicating this packing structure as a dominant feature of the Y6 bulk. Within this interacting subset, we identify a more tightly packed group of 88 configurations characterized by the presence of 25 or more close contacts. According to our criterion, these configurations with 25 or more close contacts correspond to face-on relative orientations between Y6 backbones. Consequently, face-on arrangements account for approximately 35% of the configurations exhibiting at least one close contact. This value is in good agreement with previous simulation studies, which reported a face-on population of approximately 39% using the same criterion, thereby supporting the reliability of the present multiscale modeling approach.[17]

Fig. 2 provides a comprehensive overview of the intermolecular packing diversity captured in our ensemble. Panel (a) shows the distribution of the total number of close contacts observed across the 300 configurations, with the region corresponding to face-on relative orientations clearly indicated. The broad distribution reflects the heterogeneous nature of the Y6 bulk, spanning weakly interacting dimers, intermediate packing motifs, and strongly coupled face-on configurations. Representative examples of close-contact arrangements are displayed in panels (c–f). These configurations highlight that the largest number of close contacts predominantly arises from interactions between the electron-deficient end groups and the conjugated core of neighboring molecules as demonstrated in panel (f), underscoring the role of molecular architecture in governing aggregation patterns. The presence of face-on relative orientations and π–π stacking motifs observed in these configurations is consistent with experimental studies of Y6 bulk.[9] Complementary non-covalent interaction (NCI) analyses employing the reduced density gradient (RDG) method was performed for the representative configurations in Fig. 2c–f, using Multiwfn software.[54,55] These analyses revealed predominantly weak, dispersion-dominated π–π interactions whose spatial distributions depend on the specific intermolecular packing motif as discussed in the SI.

Beyond structural characterization, the structural disorder captured in the ensemble has a pronounced impact on the intramolecular charge distribution of Y6. This effect is illustrated in panel (b) of Fig. 2, where we compare the dipole moment magnitude and the quadrupole moment component along the π–π stacking direction for the optimized geometry and for the disordered configurations sampled from the film, considering QM regions containing a single Y6 molecule. For the optimized geometry, the dipole moment magnitude is 1.46 D, whereas inclusion of disorder leads to a substantial increase to an average value of (8.3 ± 2.5) D. In contrast, the quadrupole moment along the stacking direction decreases from 100.7 D Å in the optimized structure to (58.7 ± 28.2) D Å upon inclusion of disorder. These results demonstrate that structural disorder in the bulk induces significant redistribution of electronic density within the Y6 molecule, yielding electrostatic properties that differ quantitatively from those obtained for optimized monomer geometries.

The simultaneous enhancement of dipole fluctuations and reduction of quadrupole strength highlights the sensitivity of Y6's electrostatic landscape to its local environment and disorder. This finding underscores the significant limitations of optimized-geometry models when describing the electronic properties of Y6 in the condensed phase. As shown in the following sections, these disorder-induced electrostatic fluctuations play a central role in determining ground- and excited-state properties, including exciton binding energies and their convergence with respect to QM region size.

3.2 Redox potentials

We now turn to the analysis of oxidation and reduction potentials of Y6 bulk, as well as the resulting fundamental gap defined as the difference between these two quantities. Fig. 3a summarizes the calculated redox energies obtained for the optimized geometry and for disordered bulk configurations treated within the s-QM/MM framework, considering QM regions containing one, two, three, and four Y6 molecules. All results are directly compared with available experimental values, namely an oxidation potential of −5.67 eV, a reduction potential of −3.96 eV, and a fundamental gap of 1.71 eV.[29]

As a reference, calculations performed on the optimized Y6 geometry yield oxidation and reduction potentials of −5.84 eV and −3.53 eV, respectively, corresponding to a fundamental gap of 2.31 eV. While the oxidation potential is already in reasonable agreement with experiment, the reduction potential is significantly overestimated, leading to a substantial overestimation of the fundamental gap. On the other hand, a marked improvement is observed upon inclusion of disorder effects through the s-QM/MM sampling, even when only a single Y6 molecule is treated explicitly at the quantum-mechanical level. In this case, the reduction potential shifts to (−3.84 ± 0.07) eV, much closer to the experimental value, while the oxidation potential becomes (−5.93 ± 0.07) eV. As a result, the fundamental gap is reduced to (2.09 ± 0.09) eV. These results demonstrate that structural disorder alone already captures a good description of charged states, particularly for electron addition, highlighting the critical role of conformational fluctuations in Y6 bulk. The use of vertical redox energies is further supported by our previous analysis of the closely related Y5 acceptor, for which relaxation of the charged states produced corrections of only 0.09 and 0.08 eV for oxidation and reduction, respectively.[47]

 This journal is © The Royal Society of Chemistry 2026

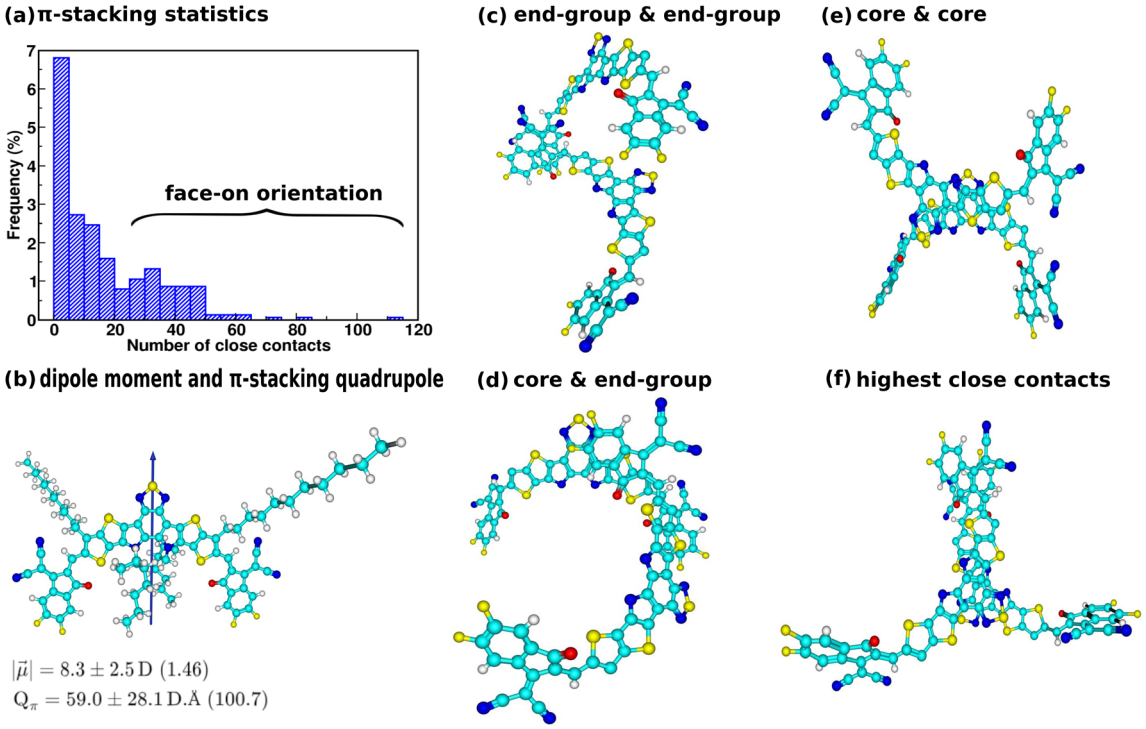

Fig. 2 Intermolecular packing, dipole moment magnitude and quadrupole moment in the π−π stacking direction of the Y6 core. (a) Distribution of the total number of close intermolecular contacts (interatomic distances ≤4.0 Å) for the 300 Y6 dimer configurations used in the QM calculations, with configurations classified as face-on relative orientation (≥25 close contacts) highlighted. (b) Dipole moment magnitude and quadrupole moment component along the π−π stacking direction for disordered bulk configurations considering single-molecule QM regions. The dipole moment vector depicted on the molecular structure corresponds to the optimized geometry, whose dipole and quadrupole moment values are also reported in parentheses. (c–f) Representative Y6 dimer packing motifs illustrating the diversity of close-contact arrangements observed in the bulk.

These values are comparable to, or substantially smaller than, the disorder-induced shifts observed here for Y6 (0.09 and 0.31 eV, respectively), particularly for the reduction energy. The consistent use of vertical energies across the ensemble also enables the effect of structural disorder to be isolated from charge-induced structural relaxation.

Further systematic improvements are obtained by increasing the size of the QM region to explicitly include intermolecular interactions and packing-induced polarization effects. When two Y6 molecules are included in the QM region, the reduction potential further stabilizes to (−3.92 ± 0.06) eV, while the oxidation potential shifts to (−5.88 ± 0.06) eV, yielding a fundamental gap of (1.96 ± 0.08) eV. Expanding the QM region to three Y6 molecules leads to additional, albeit smaller, corrections, with reduction and oxidation potentials of (−3.93 ± 0.06) eV and (−5.82 ± 0.06) eV, respectively, and a corresponding fundamental gap of (1.89 ± 0.08) eV.

A further increase to four Y6 molecules results in oxidation and reduction potentials of (−5.75 ± 0.06) eV and (−3.93 ± 0.06) eV, respectively, yielding a fundamental gap of (1.82 ± 0.09) eV. Notably, the reduction potential at this level is in essentially good agreement with the experimental value, while the oxidation potential also approaches the experimental reference. The progressive convergence of the calculated redox potentials and fundamental gap toward experimental values with increasing QM region size indicates that intermolecular electronic effects are increasingly captured as molecular packing is treated explicitly. These effects include not only polarization arising from electronic density redistribution, but also electronic coupling, wavefunction delocalization, and charge-transfer interactions between neighboring Y6 molecules. In particular, the reduction potential exhibits a clear and systematic stabilization, whereas the oxidation potential shows a more moderate but still significant dependence on the QM region size.

The resulting reduction of the fundamental gap, from 2.31 eV for the optimized geometry to (1.82 ± 0.08) eV for the largest QM region, brings the theoretical prediction into close quantitative agreement with the experimental value of 1.71 eV. Importantly, this convergence is achieved through the combined inclusion of structural disorder and explicit intermolecular interactions, highlighting the complementary roles of these effects in determining redox energetics. While disorder provides the dominant correction by stabilizing charged states, particularly for electron addition, the inclusion of larger QM regions refines this description by accounting for packing-induced polarization and electronic density redistribution.

Overall, these results demonstrate that both structural disorder and explicit intermolecular polarization are essential for a quantitatively accurate description of redox energetics in Y6 bulk. While disorder effects alone already provide

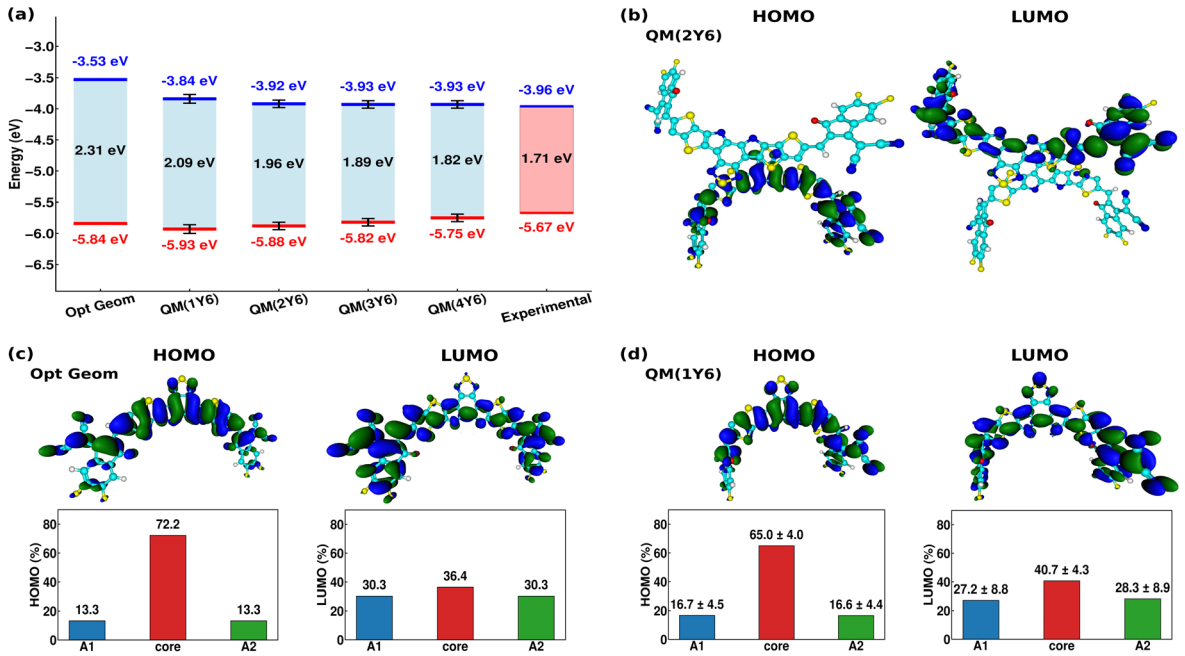

Fig. 3 Redox energetics and frontier molecular orbitals of Y6 in the bulk film. (a) Oxidation potentials (red line), reduction potentials (blue line), and fundamental gaps (light blue) were obtained for the optimized geometry (Opt Geom) and for disordered film configurations treated within the s-QM/MM framework, with QM regions containing one (QM(1Y6)), two (QM(2Y6)), three (QM(3Y6)), or four (QM(4Y6)) Y6 molecules. Experimental values are shown for comparison.[29] (b) Representative example of a Y6 dimer configuration illustrating packing-induced orbital localization, where the Kohn–Sham HOMO and LUMO are localized on different Y6 molecules, highlighting the emergence of intermolecular electronic separation in the ground state. (c) Kohn–Sham HOMO and LUMO orbitals for the optimized Y6 geometry together with the corresponding intramolecular contributions from the conjugated core and end-group units (A1 and A2), and their ensemble-averaged distributions obtained from disordered single-molecule QM configurations (d).

a substantial improvement over the optimized-geometry model, the systematic inclusion of larger QM regions further refines the energetic landscape and enables convergence toward experimental values. These findings underscore the importance of simultaneously accounting for disorder and molecular packing, and reinforce the central role of multiscale modeling in capturing the electronic properties of non-fullerene acceptors in the condensed phase. This behavior further suggests that accurate redox energetics can be achieved without requiring very large QM regions, provided that structural disorder is explicitly accounted for, highlighting the interplay between disorder and QM region size in determining electronic properties.

3.3 Frontier molecular orbitals

To gain deeper insight into the trends observed in the redox potentials, we next analyze the spatial distribution and composition of the Kohn–Sham frontier molecular orbitals of Y6 in the bulk. The localization and delocalization patterns of the highest occupied molecular orbital (HOMO) and lowest unoccupied molecular orbital (LUMO) provide an orbital-level interpretation of the energetic shifts discussed above and establish a direct link between the ground-state electronic structure and the excited-state properties addressed in the following subsection.

For the optimized geometry, the HOMO is predominantly localized on the conjugated core of the Y6 molecule, with a contribution of approximately 72%, while the end-group units (A1 and A2) account for about 27% of the orbital density (Fig. 3c). Upon inclusion of disorder effects, this picture is partially modified but not qualitatively altered. Averaged over the ensemble of disordered configurations containing a single Y6 molecule in the QM region, the HOMO contribution on the core decreases to $(65.0 \pm 4.0)\%$, while the end-group contribution (A1 and A2) increases to $(33.3 \pm 8.9)\%$. In contrast, a more pronounced disorder-induced effect is observed for the LUMO. For the optimized geometry, the LUMO is primarily localized on the end-group units with a contribution of 60.6%, with a smaller contribution from the conjugated core equal to 36.4%. Upon inclusion of disorder, the ensemble-averaged LUMO exhibits a clear redistribution of orbital density, with contributions of $(40.7 \pm 4.3)\%$ on the core and $(55.5 \pm 17.7)\%$ on the end groups. This enhanced sensitivity of the LUMO to structural fluctuations is consistent with the stronger stabilization of the reduction potential relative to the oxidation potential and highlights the role of disorder in modulating electron-accepting states in Y6 bulk.

Including an additional Y6 molecule in the QM region reveals qualitatively new features arising from molecular packing. For the dimer configurations, the HOMO and LUMO are frequently localized on different Y6 molecules within the QM cluster, as illustrated in Fig. 3b. In these cases, the HOMO resides predominantly on one molecule, whereas the LUMO is localized on a neighboring molecule, evidencing a pronounced

 This journal is © The Royal Society of Chemistry 2026

intermolecular separation of the frontier orbitals. This behavior is observed in 59% of the dimer configurations while in 28% of the configurations both frontier orbitals remain predominantly localized on the same Y6 molecule. For these cases of frontier orbitals concentrated in the same molecule, the intramolecular distribution of the HOMO and LUMO over the fused-ring core and terminal groups closely resembles that obtained for single-molecule QM calculations, indicating that molecular packing mainly influences the intermolecular localization of the frontier orbitals while largely preserving their intramolecular character. A detailed statistical analysis of the orbital localization patterns observed for the dimer configurations is provided in the SI.

The coexistence of configurations in which the HOMO and LUMO are localized on the same molecule and configurations in which they reside on different molecules represents a clear packing-induced effect on the ground-state electronic structure of Y6 bulk. This behavior reveals an intrinsic propensity for intermolecular charge-transfer character already at the frontier-orbital level, even prior to electronic excitation. Consequently, these findings suggest that excited states in Y6 aggregates may exhibit significant charge-transfer character. Taken together, these results demonstrate that disorder and molecular packing modify the electronic structure of Y6 in complementary ways. Structural disorder enhances intramolecular orbital mixing and increases fluctuations in electronic density localization, particularly for the LUMO, while explicit intermolecular interactions promote spatial separation of frontier orbitals across neighboring molecules. This combination naturally facilitates intermolecular charge-transfer processes and provides a microscopic foundation for the molecular packing effects and reduced fundamental gaps observed with increasing QM region size.

3.4 UV-Vis spectrum

To evaluate the impact of structural disorder on the optical response of Y6 bulk, a UV-Vis absorption spectrum was computed using TD-DFT excitation energies and oscillator strengths. The spectrum was obtained by Gaussian convolution of the lowest 50 vertical singlet excitations calculated for an ensemble of disordered configurations, considering a single Y6 molecule in the QM region. For comparison, an analogous spectrum was constructed using excitation energies from the optimized geometry. The resulting spectrum is shown in Fig. 4, together with the experimental absorption profile.[9]

A clear improvement in agreement with experiment is observed upon inclusion of disorder. The spectrum from the optimized geometry shows sharp features and fails to reproduce the excitation energies and, consequently, the experimental band shape. In contrast, the ensemble-averaged spectrum captures both the width and asymmetry of the main absorption band. This behavior reflects the broad distribution of excitation energies induced by structural disorder. These results demonstrate that disorder plays a central role in shaping the optical response of Y6 bulk and that optimized geometry calculations are insufficient to reproduce experimental absorption line shapes.

Despite the overall agreement, a more detailed analysis reveals specific spectral features that are not fully captured by the present approach. In particular, the experimental absorption spectrum exhibits a shoulder in the range of 700–750 nm, which has been reported in a previous study of a Y6 film.[19] In this spectral region, the calculated excitation energies display a reduced density, leading to a noticeable gap between low-lying transitions, as indicated by the vertical bars in Fig. 4. A similar behavior has been reported for related systems, such as PF5–Y5 films, where the presence of a shoulder in the absorption spectrum was associated with the separation between dominant low-energy excitations.[21] This observation suggests that additional effects, such as vibronic coupling, may contribute to the redistribution of intensity and the emergence of fine spectral features beyond what is captured by purely electronic excitations and disorder.[56] While an explicit treatment of vibronic effects is partly included with the s-QM/MM sampling in the present work, the presence of a structured excitation spectrum highlights the interplay between electronic and nuclear degrees of freedom in the optical response of Y6.

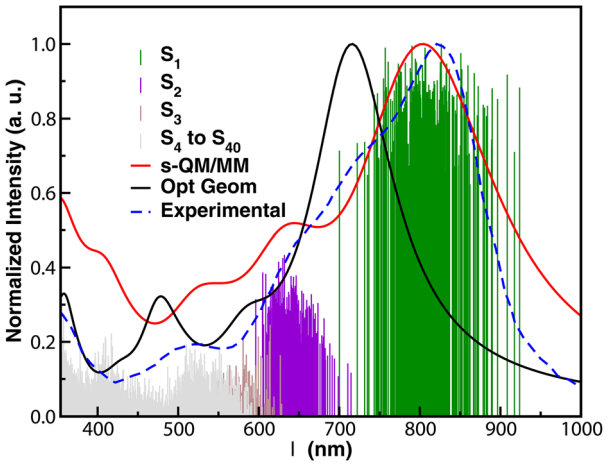

Fig. 4 UV-Vis absorption spectrum of Y6 obtained by Gaussian convolution of the lowest 50 vertical excitation energies and oscillator strengths. Shown are the spectrum computed for the optimized geometry (black line) and the ensemble-averaged spectrum (red line) obtained from disordered configurations with a single Y6 molecule in the QM region. Vertical bars represent individual electronic excitations, and the experimental absorption spectrum (dashed blue line) is included for comparison.[9]

Overall, these results demonstrate that incorporating structural disorder through ensemble averaging is essential to obtain at least partly the main features of the UV-Vis spectrum of Y6 bulk, particularly the broadening of electronic transitions and the resulting band shape. At the same time, the distribution of low-lying excitation energies provides further insight into the nature of the first excited states. In the following section, we analyze the optical gap and oscillator strength of the lowest singlet excitation in order to elucidate its character and its dependence on structural disorder and molecular packing structure.

3.5 Optical gap and oscillator strength of the first excited state

We now examine the optical gap of the Y6 bulk, defined as the vertical excitation energy of the lowest singlet excited state (S_1),

together with the corresponding oscillator strength. These quantities provide complementary insight into the excited-state electronic structure, where the optical gap reflects the energy of the first absorption feature and the oscillator strength quantifies the transition probability and its local or charge-transfer character. Fig. 5 summarizes the results for the optimized geometry and disordered bulk configurations, considering QM regions containing one, two, three, and four Y6 molecules.

For the optimized geometry, the calculated optical gap is 1.73 eV, which is significantly higher than the experimental value of 1.31 eV. This discrepancy mirrors the behavior observed for the fundamental gap and highlights the limitations of the optimized-geometry model for describing excited-state properties in the condensed phase. Upon inclusion of disorder through the multiscale sampling, a pronounced red shift is observed even when only a single Y6 molecule is treated at the quantum-mechanical level. In this case, the ensemble-averaged optical gap decreases to (1.54 ± 0.07) eV, representing a substantial improvement and underscoring the dominant role of structural disorder in stabilizing low-lying excited states in Y6 bulk. Further reductions of the optical gap are obtained by increasing the size of the QM region. When two Y6 molecules are included, the optical gap decreases to (1.50 ± 0.06) eV, while inclusion of three Y6 molecules leads to (1.48 ± 0.05) eV. A further expansion to four Y6 molecules yields an optical gap of (1.46 ± 0.05) eV, indicating continued, albeit progressively smaller, stabilization of the excited state. Although the experimental optical gap is commonly determined from the absorption onset, it is also informative to compare the calculated vertical excitation energies with the maximum of the experimental absorption spectrum. In this regard, the optical gap obtained with four Y6 molecules, (1.46 ± 0.05) eV, is in excellent agreement with the experimental absorption maximum of 1.50 eV.[9]

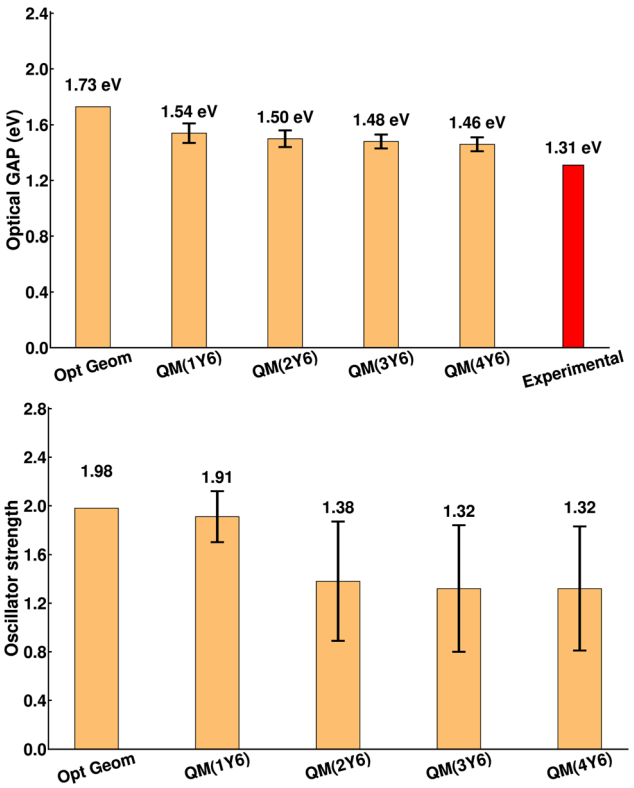

Fig. 5 Optical gap (top panel) and oscillator strength (bottom panel) of the first excited state in Y6 bulk. Optical gap, defined as the vertical excitation energy of the lowest singlet excited state, was obtained for the optimized geometry and for disordered bulk configurations treated within the sequential QM/MM framework, considering QM regions containing one (QM(1Y6)), two (QM(2Y6)), three (QM(3Y6)), and four (QM(4Y6)) Y6 molecules. The experimental value is shown for comparison.[9] Corresponding oscillator strength of the S_1 transition, illustrating the effect of structural disorder and QM region size on the transition probability and excited-state character. Error bars represent energetic disorder extracted from Gaussian fits to the ensemble distributions.

This systematic convergence toward the experimental value reflects the increasing contributions of intermolecular interactions and polarization effects, both of which are associated with the molecular packing. However, the magnitude of the corrections beyond the single-molecule QM model is relatively modest compared to the initial disorder-induced shift. This observation indicates that structural disorder provides the dominant contribution to the stabilization of the optical gap, while explicit inclusion of aggregation effects refines the energetic description.

In addition to energetic trends, the oscillator strength of the first excited state exhibits a clear and systematic evolution with both disorder and QM region size, as shown in Fig. 5. For the optimized geometry, the S_1 oscillator strength is relatively large (1.98). Upon inclusion of disorder for single-molecule QM configurations, the ensemble-averaged oscillator strength decreases to (1.91 ± 0.21), indicating a modest reduction in transition probability due to structural and electrostatic fluctuations. A more pronounced decrease is observed when intermolecular packing is explicitly included. For dimer QM regions, the oscillator strength drops to (1.38 ± 0.49), and similar values are obtained for larger QM regions, with (1.32 ± 0.52) for trimers and (1.32 ± 0.55) for tetramers. At the same time, the associated disorder increases significantly with QM region size, reflecting enhanced excited-state heterogeneity. This behavior is consistent with increased delocalization of the excited-state wavefunction across multiple molecules and the emergence of configurations with substantial intermolecular charge-transfer character, for which reduced oscillator strengths are expected.

Taken together, these results demonstrate that structural disorder plays a dominant role in lowering the optical gap of Y6 bulk, while explicit inclusion of molecular packing provides additional stabilization and significantly alters the nature of the lowest excited state. The systematic reduction and broadening of the oscillator strength with increasing QM region size indicate a growing contribution of intermolecular charge-transfer character in the S_1 state, particularly for large QM regions. These findings further support the conclusion that an accurate description of excited-state properties in Y6 bulk requires the combined treatment of disorder and molecular packing. In the following subsection, we examine this behavior in detail by analyzing the natural transition orbitals of the first excited state,

 This journal is © The Royal Society of Chemistry 2026

providing a picture of excitation localization and charge-transfer processes.

3.6 Charge-transfer character of the first excited state

To elucidate the nature of the lowest singlet excited state and rationalize the trends observed in the optical gap and oscillator strength, we analyze the charge-transfer (CT) character of the S_1 state using natural transition orbitals (NTOs). Fig. 6 summarizes the intramolecular and intermolecular intrinsic charge-transfer percentages of the S_1 state, together with representative NTOs, and hole–electron overlap isosurfaces for the optimized geometry and one selected disordered configuration with one and two Y6 molecules in the QM region. All analyses were carried out using the Multiwfn software.[54,55]

For the optimized geometry, the NTOs associated with the S_1 excitation are localized on the same Y6 molecule, leading to substantial spatial overlap. The NTO isosurfaces also reveal a redistribution of electronic density between the conjugated core and the end-group units, consistent with mainly an intramolecular CT character. Quantitatively, this behavior is reflected in an intrinsic charge-transfer percentage of 58.86%, obtained by partitioning the Y6 molecule into three fragments comprising the core and the two end groups (A1 and A2) as illustrated in Fig. 6. Including structural disorder while retaining a single Y6 molecule in the QM region leads to noticeable distortions of the NTOs, reflecting sensitivity to conformational fluctuations. However, the overall localization pattern remains largely unchanged. The overlap isosurfaces become smaller and more fragmented, indicating reduced spatial coherence of the excitation. This behavior is quantitatively confirmed by an ensemble-averaged intrinsic charge-transfer percentage of $(57.30 \pm 1.54)\%$, demonstrating that structural disorder alone does not significantly enhance the CT character of the lowest excited state when only a single molecule is treated at the quantum-mechanical level.

A qualitatively different behavior emerges upon inclusion of molecular packing effects through the expanded QM region. For dimer configurations extracted from the disordered ensemble, the hole and electron NTOs frequently localize on different Y6 molecules within the QM region, as illustrated in Fig. 6. In such cases, the spatial separation between hole and electron is substantial, and the corresponding overlap isosurfaces are markedly reduced, providing direct evidence of intermolecular charge-transfer excitation. The NTO isosurfaces further corroborate this interpretation, revealing pronounced electronic density transfer between neighboring molecules rather than within a single molecular unit. When the same intramolecular partitioning scheme used for the single molecule analysis is applied to dimer configurations, the partition results in six fragments comprising the two core units and four end-

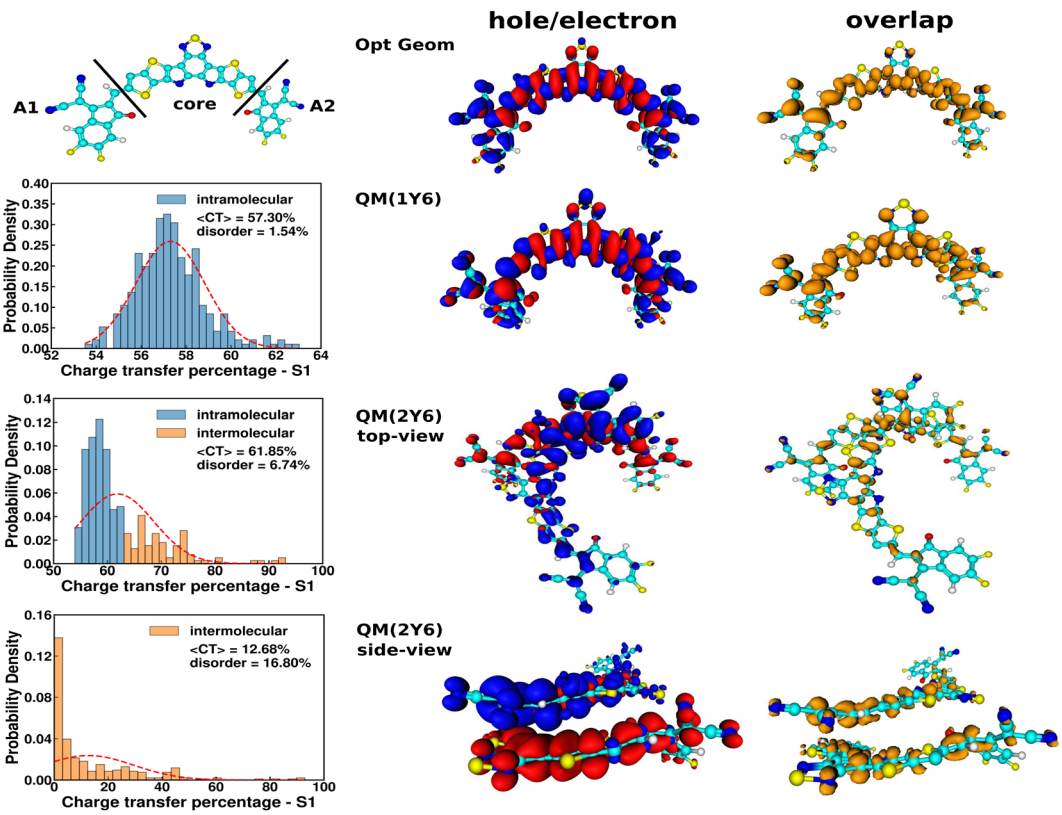

Fig. 6 Intramolecular and intermolecular intrinsic charge-transfer percentages of the S_1 state (left panels), along with representative isosurfaces of natural transition orbitals representing the hole (red) and electron (blue), hole–electron overlap (orange), for the optimized geometry (Opt Geom) and one representative disordered configuration (QM(1Y6) and QM(2Y6)). The impact of the aggregation is highlighted with the top- and side-view.

group units. In this case, the intrinsic charge-transfer percentage reflects contributions from both intramolecular and intermolecular charge transfer. Employing this partition, the ensemble-averaged intrinsic charge-transfer percentage increases to (61.85 ± 6.74)%, indicating both an enhanced average CT character and a substantially broader distribution. Since the monomer calculations yield an average intrinsic charge-transfer percentage of 57.30%, values exceeding this reference can be interpreted as indicating the presence of an additional intermolecular charge-transfer contribution. Configurations satisfying this criterion are highlighted in orange in Fig. 6. To explicitly quantify the intermolecular CT character suggested by this analysis, the fragments were subsequently redefined as the two individual Y6 molecules within each dimer. This partition yields an average intermolecular charge-transfer percentage of (12.68 ± 16.80)%, reflecting a highly heterogeneous ensemble in which a small subset of configurations exhibits pronounced intermolecular CT character.

To identify the structural motifs responsible for these highly charge-transfer-active configurations, we correlated the intermolecular charge-transfer percentage with the type of intermolecular contacts and molecular packing structure. Among the 300 dimer configurations analyzed, eight exhibited intermolecular charge-transfer percentages greater than 50%, indicating strong charge separation. These configurations are presented in the SI. Although this subset represents only a small fraction of the ensemble, it provides valuable insight into the microscopic origin of intermolecular charge-transfer states. The analysis reveals that the mere presence of close intermolecular contacts is not sufficient to explain the occurrence of strong intermolecular charge-transfer. In particular, end-group–end-group contacts are generally absent in the high-CT dimers, while core–core interactions alone do not provide a consistent descriptor, indicating that π–π stacking of the conjugated cores is not, by itself, sufficient to induce pronounced charge separation. Instead, a clear structural motif emerges in six of the eight high-CT configurations: the electron-donating region of one Y6 molecule lies near an electron-accepting region of a neighboring Y6 molecule. This donor–acceptor packing structure, rather than the existence of specific close contacts, appears to be the key factor promoting intermolecular charge-transfer. Such an orientation facilitates spatial separation of the hole and electron across different molecules and gives rise to a pronounced CT character of the S_1 state.

These findings indicate that intermolecular charge-transfer in Y6 bulk is not simply driven by molecular packing or co-facial stacking, but rather depends critically on specific relative orientations between donor and acceptor regions of neighboring molecules. Although such configurations represent only a small fraction of the disordered ensemble, they may play a disproportionately important role in determining the photophysical properties of the material. In particular, the presence of these charge-transfer-active motifs suggests that aggregation patterns promoting the donor–acceptor packing structure can enhance the intermolecular CT character of low-lying excited states in Y6 thin films, potentially facilitating charge separation processes. Exciton migration through the film may allow these relatively rare motifs to act as local charge-separation pathways and thereby contribute significantly to charge generation. However, quantitatively establishing their impact on device efficiency would require explicit modeling of exciton diffusion and charge-separation kinetics. This interpretation is consistent with recent experimental observations highlighting the importance of donor–acceptor packing motifs for efficient photoinduced charge generation in Y6-based thin films.[30]

3.7 Exciton binding energies

Having established the behavior of both the fundamental and optical gaps across different levels of structural complexity, we now turn to the exciton binding energy, defined as the difference between these two quantities. This property provides a direct measure of the strength of the electron–hole Coulomb interaction and represents a key parameter governing exciton dissociation in organic semiconductors.

The exciton binding energies obtained for the different QM regions considered in this work are summarized in Fig. 7. For the optimized geometry, we obtain an exciton binding energy of 0.58 eV, which decreases slightly to (0.55 ± 0.04) eV upon inclusion of structural disorder while retaining a single Y6 molecule in the QM region. Upon explicit inclusion of molecular packing effects through larger QM regions, a systematic reduction of the exciton binding energy is observed, yielding (0.46 ± 0.05) eV for the QM(2Y6) region, (0.41 ± 0.06) eV for QM(3Y6), and (0.36 ± 0.08) eV for QM(4Y6). This monotonic decrease reflects the increasing degree of electronic delocalization and intermolecular screening associated with aggregation, which progressively weakens the coulombic binding between the electron and hole.

Comparison with experimental estimates, typically reported in the range of 0.25–0.34 eV for Y6 thin films, shows that the

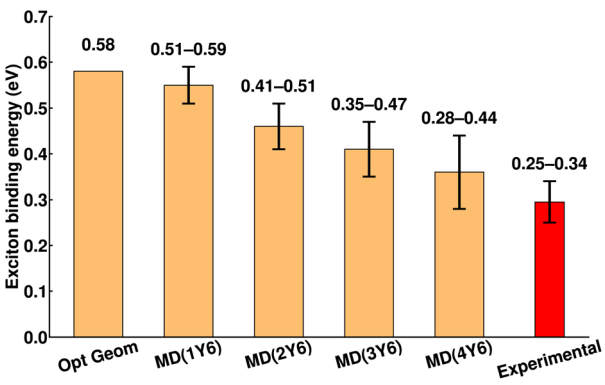

Fig. 7 Exciton binding energies (orange bars) of Y6 bulk computed as the difference between the fundamental and optical gaps for the optimized geometry and for disordered configurations with increasing QM region size (QM(1Y6), QM(2Y6), QM(3Y6), and QM(4Y6)). Bars represent ensemble-averaged values, while error bars indicate energetic disorder extracted from Gaussian fits to the corresponding probability density distributions, following the same procedure employed for the optical and fundamental gaps. The red bar denotes the experimental range reported for Y6 films.[57,58]

 This journal is © The Royal Society of Chemistry 2026

optimized geometry and single molecule-based models significantly overestimate the exciton binding energy.[57,58] In contrast, the inclusion of molecular packing effects progressively reduces the exciton binding energy, with the QM(4Y6) region yielding values in good agreement with experimental observations. Nevertheless, the continued decrease from QM(3Y6) to QM(4Y6) indicates that strict convergence with respect to QM-region size cannot be established from the present calculations. Rather, the observed trend indicates convergence toward the experimental range, while additional neighboring molecules may provide further quantitative refinement. These results provide a clear microscopic interpretation of exciton stabilization in Y6 bulk. Structural disorder alone induces minor changes in the exciton binding energy obtained for the smallest QM region (QM(1Y6)), despite its significant impact on the results obtained with the larger QM region (QM(4Y6)) and on both the fundamental and optical gaps. In contrast, explicit intermolecular interactions play a dominant role by enabling charge delocalization, thereby reducing the electron–hole Coulomb interaction.

In summary, these findings reinforce that an accurate description of exciton binding in Y6 bulk requires the simultaneous proper modelling of structural disorder and molecular packing structure. While disorder governs the distribution of electronic states, the molecular packing structure partially controls their spatial delocalization and interaction, ultimately determining excitonic properties. This interplay highlights the necessity of multiscale modeling approaches for predictive simulations of non-fullerene acceptor materials.

4 Conclusions

In this work, we presented a multiscale investigation of the electronic properties of Y6 bulk, combining molecular dynamics, sequential QM/MM calculations, and optimally tuned range-separated hybrid methods. Our results demonstrate that structural disorder plays a dominant role in shaping the electronic landscape, driving the broadening of excitation energies and significantly improving agreement with experimental redox potentials, fundamental gap, and the optical spectrum. In contrast, explicit inclusion of molecular packing further refines the description of these properties by enabling intermolecular polarization and electronic delocalization, which are essential for accurately describing the optical gap and exciton binding energies. Notably, good agreement with experimental exciton binding energies is achieved with a QM region comprising fewer molecules than previously suggested. While explicit intermolecular interactions within the QM region play a dominant role in reducing the exciton binding energy, structural disorder broadens its distribution, leading to partial overlap between the calculated and experimental ranges. Analysis of excited states further reveals the emergence of intermolecular CT character upon explicit inclusion of a neighboring Y6 molecule in the QM region, driven by specific donor–acceptor packing motifs. This work provides a framework linking disorder, packing, and electronic structure, highlighting the importance of molecular packing in governing charge-generation processes and offering a robust strategy for predictive modeling of non-fullerene acceptor materials.

Author contributions

All authors contributed equally.

Conflicts of interest

The authors declare that they have no known competing financial interests or personal relationships that could have appeared to influence the work reported in this paper.

Data availability

The data supporting the findings of this study are available in the supplementary information (SI) accompanying this article. Additional data are available upon request. Supplementary information is available. See DOI: https://doi.org/10.1039/d6ta06533c.

Acknowledgements

We acknowledge the Carl Trygger Foundation (Grant No. CTS 23:2987) and STandUP for Energy Collaboration for the financial support. The computations were enabled by resources provided by the National Academic Infrastructure for Supercomputing in Sweden (NAISS) and the Swedish National Infrastructure for Computing (SNIC) at the National Supercomputer Centre (NSC) at Linköping University, partially funded by the Swedish Research Council through Grant Agreement No. 2022-06725 and 2018-05973.

References

1 N. Yang, S. Zhang, Y. Cui, J. Wang, S. Cheng and J. Hou, *Nat. Rev. Mater.*, 2025, 1–21.
2 L. Zhu, M. Zhang, Z. Zhou, W. Zhong, T. Hao, S. Xu, R. Zeng, J. Zhuang, X. Xue, H. Jing, *et al.*, *Nat. Rev. Electr. Eng.*, 2024, **1**, 581–596.
3 J. Wang, Y. Xie, K. Chen, H. Wu, J. M. Hodgkiss and X. Zhan, *Nat. Rev. Phys.*, 2024, **6**, 365–381.
4 J. Luke, E. J. Yang, C. Labanti, S. Y. Park and J.-S. Kim, *Nat. Rev. Mater.*, 2023, **8**, 839–852.
5 M. Du, N. Sun, H. Cheng, X. Liu, X. Yi, Q. Guo, Q. Guo, M. Lv, J. Yao, L. Hu, Z. Li, Z. Zheng, C. Shan, A. K. K. Kyaw, G. Li, Q. Xia, H. Zuilhof and E. Zhou, *Angew. Chem., Int. Ed.*, 2025, **64**, e202515114.
6 J. Zhu, R. Zeng, E. Zhou, C. Li, J. Deng, M. Du, Q. Guo, M. Ji, Z. Wang, Y. Lin, F. Han, J. Zhuang, S. Tan, L. Kan, L. Zhu, M. Zhang and F. Liu, *J. Am. Chem. Soc.*, 2025, **147**, 24491–24501.
7 T. Dai, N. Sun, X. Guo, Y. Meng, Z. Jin, H. Cheng, M. Du, C. Shan, A. K. K. Kyaw, Y. Lei, *et al.*, *Sci. China:Chem.*, 2026, 1–9.

8 L. Feng, J. Yuan, Z. Zhang, H. Peng, Z.-G. Zhang, S. Xu, Y. Liu, Y. Li and Y. Zou, *ACS Appl. Mater. Interfaces*, 2017, **9**, 31985–31992.

9 J. Yuan, Y. Zhang, L. Zhou, G. Zhang, H.-L. Yip, T.-K. Lau, X. Lu, C. Zhu, H. Peng, P. A. Johnson, *et al.*, *Joule*, 2019, **3**, 1140–1151.

10 J. Yuan and Y. Zou, *Org. Electron.*, 2022, **102**, 106436.

11 S. Zhong, B. K. Yap, Z. Zhong and L. Ying, *Crystals*, 2022, **12**, 168.

12 S. M. Pratik, S. Saiev, J.-L. Brédas and V. Coropceanu, *Adv. Mater.*, 2026, e23671.

13 S. Mahadevan, T. Liu, S. M. Pratik, Y. Li, H. Y. Ho, S. Ouyang, X. Lu, H.-L. Yip, P. C. Chow, J.-L. Brédas, *et al.*, *Nat. Commun.*, 2024, **15**, 2393.

14 P. A. Hume, M. B. Price and J. M. Hodgkiss, *JACS Au*, 2024, **4**, 1295–1302.

15 R. J. E. Westbrook, A. J. Levin, W. Gao, U. Bothra, S. M. Pratik, B. Fan, F. R. Lin, Q.-Q. Zhang, K. Ngo, W. Kaminsky, J.-L. Brédas, V. Coropceanu, A. K.-Y. Jen, M. F. Toney and D. S. Ginger, *J. Am. Chem. Soc.*, 2025, **147**, 30199–30209.

16 L. J. Hart, D. G. Medranda, S. W. Yuan, L. Lindh, J. S. Müller, H. Yang, H. Gerard, T. Zhao, A. Quesada-Ramirez, M. Campoy-Quiles, *et al.*, *Nat. Mater.*, 2026, 1–10.

17 G. Kupgan, X. Chen and J. Brédas, *Mater. Today Adv.*, 2021, **11**, 100154.

18 D. Yuk, M. H. Jee, C. W. Koh, W.-W. Park, H. S. Ryu, D. Lee, S. Cho, S. Rasool, S. Park, O.-H. Kwon, J. Y. Kim and H. Y. Woo, *Small*, 2023, **19**, 2206547.

19 X. Zou, G. Wen, R. Hu, G. Dong, C. Zhang, W. Zhang, H. Huang and W. Dang, *Molecules*, 2020, **25**, 4118.

20 G. Wen, R. Hu, X. Su, Z. Chen, C. Zhang, J. Peng, X. Zou, X. He, G. Dong and W. Zhang, *Dyes Pigm.*, 2021, **192**, 109431.

21 L. R. Franco, D. Valverde, C. Marchiori, E. Moons, E. Wang and C. M. Araujo, *J. Phys.: Energy*, 2025, **7**, 045001.

22 H. Tamura, *J. Chem. Phys.*, 2025, **162**, 054712.

23 S. J. Akram, S. Meißner and S. Kümmel, *Adv. Funct. Mater.*, 2025, 2419236.

24 M. e. Frisch, G. Trucks, H. B. Schlegel, G. Scuseria, M. Robb, J. Cheeseman, G. Scalmani, V. Barone, G. Petersson, H. Nakatsuji *et al.*, *Gaussian 16*, 2016.

25 C. M. Breneman and K. B. Wiberg, *J. Comput. Chem.*, 1990, **11**, 361–373.

26 W. L. Jorgensen and J. Tirado-Rives, *Proc. Natl. Acad. Sci. U. S. A.*, 2005, **102**, 6665–6670.

27 L. S. Dodda, I. Cabeza de Vaca, J. Tirado-Rives and W. L. Jorgensen, *Nucleic Acids Res.*, 2017, **45**, W331–W336.

28 L. Martínez, R. Andrade, E. G. Birgin and J. M. Martínez, *J. Comput. Chem.*, 2009, **30**, 2157–2164.

29 J. Bertrandie, J. Han, C. S. P. De Castro, E. Yengel, J. Gorenflot, T. Anthopoulos, F. Laquai, A. Sharma and D. Baran, *Adv. Mater.*, 2022, **34**, 2202575.

30 A. Kumar, R. J. Hudson, N. A. Shumilov, C.-Y. Lin, T. A. Smith, N. J. L. K. Davis, E. C. Le Ru, M. B. Price, P. A. Hume and J. M. Hodgkiss, *J. Phys. Chem. Lett.*, 2025, **16**, 1367–1375.

31 M. J. Abraham, T. Murtola, R. Schulz, S. Páll, J. C. Smith, B. Hess and E. Lindahl, *SoftwareX*, 2015, **1–2**, 19–25.

32 G. Bussi, D. Donadio and M. Parrinello, *J. Chem. Phys.*, 2007, **126**, 014101.

33 M. Bernetti and G. Bussi, *J. Chem. Phys.*, 2020, **153**, 114107.

34 T. Darden, D. York and L. Pedersen, *J. Chem. Phys.*, 1993, **98**, 10089–10092.

35 B. Hess, H. Bekker, H. J. C. Berendsen and J. G. E. M. Fraaije, *J. Comput. Chem.*, 1997, **18**, 1463–1472.

36 K. Coutinho and S. Canuto, in *Solvent Effects from a Sequential Monte Carlo – Quantum Mechanical Approach*, ed. P.-O. Löwdin, J. R. Sabin, M. C. Zerner, J. Karwowski and M. Karelson, Advances in Quantum Chemistry, Academic Press, 1997, vol. 28, pp. 89–105.

37 K. Coutinho, R. Rivelino, H. C. Georg and S. Canuto, in *The Sequential qm/mm Method and its Applications to Solvent Effects in Electronic and Structural Properties of Solutes*, Springer Netherlands, Dordrecht, 2008, pp. 159–189.

38 C. E. Tzeliou, M. A. Mermigki and D. Tzeli, *Molecules*, 2022, **27**, 2660.

39 G. Zhang, X.-K. Chen, J. Xiao, P. C. Chow, M. Ren, G. Kupgan, X. Jiao, C. C. Chan, X. Du, R. Xia, *et al.*, *Nat. Commun.*, 2020, **11**, 3943.

40 T. Halevi, T. A. L. Romain, P. A. Hume, P. N. Horton, S. J. Coles, R. L. Harniman, A. Blandford, J. A. Smith, R. Cousins, D. Alibhai, A. J. Orr-Ewing, S. R. Hall and M. B. Price, *J. Am. Chem. Soc.*, 2026, **148**, 28881–28892.

41 R. Kerremans, C. Kaiser, W. Li, N. Zarrabi, P. Meredith and A. Armin, *Adv. Opt. Mater.*, 2020, **8**, 2000319.

42 T. M. Henderson, A. F. Izmaylov, G. Scalmani and G. E. Scuseria, *J. Chem. Phys.*, 2009, **131**, 044108.

43 S. Bhandari, M. S. Cheung, E. Geva, L. Kronik and B. D. Dunietz, *J. Chem. Theory Comput.*, 2018, **14**, 6287–6294.

44 S. Refaely-Abramson, S. Sharifzadeh, M. Jain, R. Baer, J. B. Neaton and L. Kronik, *Phys. Rev. B:Condens. Matter Mater. Phys.*, 2013, **88**, 081204.

45 L. Kronik and J. B. Neaton, *Annu. Rev. Phys. Chem.*, 2016, **67**, 587–616.

46 M. A. Rohrdanz, K. M. Martins and J. M. Herbert, *J. Chem. Phys.*, 2009, **130**, 054112.

47 L. R. Franco, C. Marchiori and C. M. Araujo, *J. Chem. Phys.*, 2023, **159**, 204110.

48 G. Kupgan, X.-K. Chen and J.-L. Brédas, *ACS Mater. Lett.*, 2019, **1**, 350–353.

49 T. Körzdörfer, J. S. Sears, C. Sutton and J.-L. Brédas, *J. Chem. Phys.*, 2011, **135**, 204107.

50 T. B. de Queiroz and S. Kümmel, *J. Chem. Phys.*, 2014, **141**, 084303.

51 M. Brütting, H. Bahmann and S. Kümmel, *J. Chem. Phys.*, 2024, **160**, 181101.

52 S. Fürst, M. Haasler, R. Grotjahn and M. Kaupp, *J. Chem. Theory Comput.*, 2023, **19**, 488–502.

53 M. Brütting, J. M. Foerster and S. Kümmel, *J. Phys. Chem. Lett.*, 2023, **14**, 3092–3102.

54 T. Lu and F. Chen, *J. Comput. Chem.*, 2012, **33**, 580–592.

55 T. Lu, *J. Chem. Phys.*, 2024, **161**, 082503.

 This journal is © The Royal Society of Chemistry 2026

56 S. Giannini, D. J. Sowood, J. Cerdá, S. Frederix, J. Grüne, G. Londi, T. Marsh, P. Ghosh, I. Duchemin, N. C. Greenham, K. Vandewal, G. D'Avino, A. J. Gillett and D. Beljonne, *Mater. Today*, 2024, **80**, 308–326.
57 D. Neusser, B. Sun, W. L. Tan, L. Thomsen, T. Schultz, L. Perdigón-Toro, N. Koch, S. Shoaee, C. R. McNeill, D. Neher and S. Ludwigs, *J. Mater. Chem. C*, 2022, **10**, 11565–11578.
58 A. Sugie, K. Nakano, K. Tajima, I. Osaka and H. Yoshida, *J. Phys. Chem. Lett.*, 2023, **14**, 11412–11420.